Journal of Alloys and Compounds 1014 (2025) 178584

Contents lists available at ScienceDirect

Journal of Alloys and Compounds

journal homepage: www.elsevier.com/locate/jalcom

Cytocompatible and antibacterial efficacy of surface designed $Ti_{40}Cu_{40}Zr_{11}Fe_3Sn_3Ag_3$ amorphous alloy for potential biomedical applications

Kirti Tiwari [a], Andreu Blanquer [b], David Zermeño Pérez [c,d], Cristina Pavan [e,f], Maura Tomatis [e,g], Nora Fernandez Navas [h,i], Federico Scaglione [a], Brian J. Rodriguez [d], Annett Gebert [h], Francesco Turci [e,*], Tadhg Ó Cróinín [c], Carme Nogués [b,**], Paola Rizzi [a]

[a] Department of Chemistry and NIS, Università degli Studi di Torino, Torino 10125, Italy
[b] Departament de Biologia Cel·lular Fisiologia i Immunologia Universitat Autònoma de Barcelona Edifici C, Bellaterra 08193, Spain
[c] School of Biomolecular and Biomedical Science, University College Dublin, Dublin 4, Ireland
[d] School of Physics, University College Dublin, Belfield, Dublin 4, Ireland
[e] Department of Chemistry, "G. Scansetti" Interdepartmental Centre for Studies on Asbestos and Other Toxic Particulates, Università degli Studi di Torino, Torino 10125, Italy
[f] Louvain Centre for Toxicology and Applied Pharmacology, Institute of Experimental and Clinical Research, Université catholique de Louvain, Brussels 1200, Belgium
[g] Department of Veterinary Sciences, Università degli Studi di Torino, Grugliasco 10095, Italy
[h] Leibniz-Institute for Solid State and Materials Research Dresden (Leibniz IFW Dresden), Helmholtzstr. 20, Dresden 01069, Germany
[i] Faculty of Mechanical Science and Engineering, TU Dresden, Helmholtzstr. 10, Dresden 01069, Germany

ARTICLE INFO

Keywords:
Amorphous Alloy
Surface Treatment
Cytocompatibility
Antibacterial Activity
Reactive Oxygen Species

ABSTRACT

This study explores the feasibility of utilizing chemically treated $Ti_{40}Cu_{40}Zr_{11}Fe_3Sn_3Ag_3$ at% amorphous alloy as a potential implant material. This work involves synthesis of nano-structured surfaces using chemical *pseudo-dealloying* by employing an ammonia-based solution (NH_4OH and H_2O_2). Two distinct surfaces were developed by modifying solution concentration and in vitro cytocompatibility and antibacterial response of the treated ribbon samples were assessed. The findings reveal that the modified Ti-based amorphous alloy is cytocompatible with Saos-2 and HOb cells and exhibits antibacterial activity against the clinically relevant gram-negative pathogen *Pseudomonas aeruginosa*. Moreover, the modified surfaces can induce the release of reactive oxygen species, such as hydroxyl radicals, in a cell-free medium simulating an inflammatory system, suggesting a potential antibacterial response.

1. Introduction

Over the years, various biomedical implants, such as stainless steel, commercially pure titanium (Ti), zirconium (Zr), Ti-based alloys (e.g., Ti6Al4V), and Co/Mg-based alloys, have been developed to meet specific medical needs [1]. Among them, Ti-based implants are widely used due to their excellent biocompatibility, mechanical strength, and ability to promote osseointegration [2–4]. These properties are critical for orthopedic and dental applications, where strong bonding between the implant and bone is necessary. However, Ti-based crystalline implants face challenges such as mechanical failures (fatigue and wear), corrosion, and biofilm-related infections [5–8].

Biofilm-related infections are another major concern. Bacterial biofilms, protected by extracellular polymeric matrices, are highly resistant to antibiotics, leading to chronic infections that often require revision surgeries, increasing economic burdens and mortality [9–13]. Addressing these issues requires the development of materials with superior mechanical properties, biocompatibility, and antibacterial capabilities. Amorphous alloys (metallic glasses) have emerged as promising candidates due to their disordered atomic structure, which enables unique properties such as high strength, hardness, wear resistance, and a lower Young's modulus [14,15]. Ti-based amorphous alloys containing elements such as Ti, Zr, and Cu have shown promising mechanical properties and biocompatibility [16,17].

* Corresponding author.
** Correspondence to: Departament Biologia Cel·lular, Fisiologia i Immunologia, Unitat Biologia Cel·lular, Campus, de la UAB, Barcelona, Bellaterra 08193, Spain
E-mail addresses: francesco.turci@unito.it (F. Turci), carme.nogues@uab.cat (C. Nogués).

https://doi.org/10.1016/j.jallcom.2025.178584
Received 8 September 2024; Received in revised form 18 December 2024; Accepted 8 January 2025
Available online 10 January 2025
0925-8388/© 2025 The Author(s). Published by Elsevier B.V. This is an open access article under the CC BY-NC-ND license (http://creativecommons.org/licenses/by-nc-nd/4.0/).

Amorphous alloys with a combination of compositions containing valve metals such as (Ti, Cu, Zr)$_{92.5}$Fe$_{2.5}$Sn$_2$Si$_1$Ag$_2$ [18], Ti$_{47}$Cu$_{38-X}$Zr$_{7.5}$Fe$_{2.5}$Sn$_2$Si$_1$Ag$_2$Nb$_X$ (x = 0, 1, 2 at%) [19], Ti$_{47}$Cu$_{38-X}$Zr$_{7.5}$Fe$_{2.5}$Sn$_2$Si$_1$Ag$_2$Pd$_X$ (x = 1, 2, 3, and 4 at%) [20] and (Ti, Zr, Cu)$_{94.5}$Fe$_{2.5}$Sn$_2$Si$_1$ [21] have shown promising cytocompatibility with mouse MC3T3-E1 pre-osteoblast cell line indicating the potential of these compositions for biomedical implant application. It is important to consider the presence of copper (Cu) in these compositions. It is known that Cu is crucial for enhancing the glass forming ability of the Ti-based alloys [22,23], whereas its presence in high concentration can cause cytotoxicity, especially in long term implantation. In a study by Lin et al. [24] reported that while low-Cu Ti-based metallic glasses exhibited excellent corrosion resistance and low cytotoxicity, high-Cu alloys showed ion release, pitting corrosion, and poor cell viability, warranting further investigation for long-term biocompatibility. Osteoblasts, derived from osteoprogenitor cells, play a key role in bone formation and mineralization. Their cytocompatibility response is critical for evaluating the suitability of biomaterials for orthopedic applications.

While numerous investigations focus on assessing cytocompatibility, there is limited research on the antibacterial activity of amorphous alloys [25]. Addressing biofilm-related infections is crucial, and current research emphasizes surface modification techniques, including both physical and chemical modifications [26,27]. Tailoring surface properties, including roughness, wettability, and chemical composition, can enhance the biocompatibility and antibacterial response of implants [28,29]. Alternative approaches for bacterial prevention on implant surfaces involve contact killing, utilizing antimicrobial elements like Zn, Ga, Cu, Ag [30–36]. Notably, biomaterials based on Cu have shown significant advancements, demonstrating both antibacterial and osteogenic properties [37].

The antibacterial activity of Cu involves damage to bacterial membranes, oxidation of proteins, and DNA degradation, often mediated by reactive oxygen species (ROS) [38–40]. Secondly, the toxicity of Cu ions is associated with their ability to catalyze Fenton chemistry, leading to the generation of reactive oxygen species (ROS). ROS can cause irreversible damage to cellular components and disrupt the normal functioning of the bacterial cells. This oxidative damage can inhibit the respiratory chain, divert electrons, and further enhance ROS production, resulting in a cascade of detrimental effects on the bacteria [41,42].

Numerous researchers have integrated Cu through either elemental alloying or functionalized surface coating. Recent investigations have delved into integrating Cu as an alloyed element, including Ti alloys such as Ti6Al4V. Results indicate that alloys containing Cu display heightened antibacterial properties compared to conventional commercially pure titanium (cp-Ti). In cp-Ti, biofilm formation is commonly observed among bacterial strains like *S. aureus*, *P. aeruginosa*, and *E. coli* [43–48]. Wan et al. [49] reported that Cu ion implantation on 317 SSL (stainless steel), cp-Ti and Ti6Al7Nb alloy improved the antibacterial activity against *S. aureus* indicating benefit of Cu regardless of the substrate type. Arroussi et al. [50] added 5 wt% of Cu to cp-Ti and found that Cu ions released from the alloy are effective against *P. aeruginosa* after 24 h of incubation.

Despite the benefits of Cu for antibacterial activity, balancing effective antibacterial properties and minimal cytotoxicity remains a challenge. Materials must combat biofilm-related infections while ensuring host safety. Surface dealloying or selective element etching technique present a promising approach for modifying Ti-Cu-based amorphous alloys [51,52]. However, due to rapid surface oxidation of Ti and Zr, dealloying in these systems is often limited to a thin surface layer, termed *pseudo-dealloying* due to the compositional and morphological changes that are confined to a surface layer and that are not altering the whole material thickness [53,54].

In our previous work [55], we demonstrated the promising potential of Ti$_{40}$Cu$_{40}$Zr$_{11}$Fe$_3$Sn$_3$Ag$_3$ at% amorphous alloy as candidate material for biomedical applications. By employing an alkaline pseudo-dealloying treatment using ammonium hydroxide (NH_4OH) and hydrogen peroxide (H_2O_2), the surface morphology and composition of the alloy was successfully modified. This process led to the formation of a nanostructured, titanium/zirconium oxide-enriched surface with traces of copper at the near-surface region while the bulk remained metallic in nature. The treated surfaces, with a maximum thickness of hundreds of nm, exhibited hydrophilic behavior, enhanced roughness, and excellent hemocompatibility, with hemolysis rates below 1.5 %, classifying them as non-hemolytic according to ASTM standards. Building on these findings, among all the materials produced in the previous work, the most promising were selected in the work, that is now extended to further investigate the biocompatibility of the material by ensuring a non-cytotoxic environment for osteoblast cells. Additionally, the antibacterial response of the treated surfaces was explored, addressing a critical need for implant materials that can prevent bacterial colonization and biofilm formation while supporting cellular proliferation and tissue integration.

2. Materials and methods

2.1. Sample preparation and characterization

A master alloy ingot with a composition of Ti$_{40}$Cu$_{40}$Zr$_{11}$Fe$_3$Sn$_3$Ag$_3$ at % was fabricated through arc melting using pure elements (Ti 99.99 %, Cu 99.99 %, Zr 99.5 %, Sn 99.99 %, Fe 99.95 %, and Ag 99.99 %) in an argon inert atmosphere employing an Edmund Buhler AM-200 arc melting apparatus. The pure elements underwent eight consecutive arc-melting cycles to ensure thorough homogenization. Subsequently, the master alloy was subjected to melt-spinning using a Melt Spinner SC apparatus. This process involved induction heating to melt the alloy in a boron nitride crucible, followed by the ejection of the molten liquid at a temperature of 1100°C. The ejection was carried out with an overpressure of Δp 0.3 bar onto a rotating Cu wheel at a speed of 30 m/s. The entire process took place in an argon atmosphere maintained at 1 bar pressure. The resulting as-quenched ribbons exhibited dimensions of 4 mm in width and 50 μm in thickness [55]. To facilitate experiments requiring large surface areas, we produced and studied ribbons. Although the composition can form bulk metallic glass due to its high glass-forming ability, the surface changes observed in the ribbons are expected to be the same as those in bulk form.

The analysis of the structure of the as-quenched ribbon was conducted through X-ray diffraction (XRD, Panalytical X'Pert apparatus) under the tension of 40 kV and current of 30 mA, utilizing a slit size of 1/4 degree and a 5 mm aperture, with a step size of 0.0167 and a scan speed of 600 counts. Continuous scan mode was utilized using a Cu Kα radiation (λ=1.5418 Å) in Bragg Brentano geometry. The thermal characteristics of the as-quenched ribbon was assessed via a differential scanning calorimeter (DSC Perkin Elmer DSC 8000) employing a heating rate of 20 °C/min, within the temperature range of 50 °C to 650 °C, while maintaining an argon atmosphere.

Nanostructured surfaces were fabricated using chemical *pseudo-dealloying* of amorphous alloy. The ribbon samples were ultrasonically cleaned with acetone and ethanol for 5 min respectively, followed by air drying. The cleaned ribbon samples were subjected to etching in a Pyrex glass beaker containing a mixture of ammonium hydroxide (NH_4OH, 25 %, Merck), hydrogen peroxide (H_2O_2, 30 %, Merck), and deionized water (H_2O) with two different concentrations. The first solution, referred to as diluted ammonia solution (DS), was prepared by mixing NH_4OH, H_2O_2, and H_2O in a 5:1:4 vol ratio. The second solution, known as the concentrated ammonia solution (CS), was prepared by combining equal parts of NH_4OH and H_2O_2 in a 1:1 vol ratio. The ribbon samples were immersed for 60 min in electrolyte, and, after etching, the ribbon samples were washed five times using DI H_2O, followed by an oven drying at 50 °C for 2 h. The surface morphology of the two ribbon samples was analyzed using Field Emission Scanning Electron Microscopy (FESEM Tescan S 9000 G) at 100kx and 500kx magnification and 10 keV energy using secondary electron detectors. Image J software

(NIH) was used for calculating surface pore and ligament sizes with a minimum of 40 points.

Surface wettability was assessed with the Theta lite optical tensiometer and oneAttension software (Biolin Scientific) in a sessile drop configuration, employing a 3 μL droplet of DI H_2O and recorded after one second. The measurements were conducted in triplicate, involving three drops on each freshly prepared sample (n = 9).

The surface composition was analyzed using X-ray Photoelectron Spectroscopy (XPS) with sputter depth profiling using an Argon ion gun (SPECS) in a 100 mm hemispherical analyzer. A non-monochromatic Mg-Kα X-ray source at 400 W and 15 kV was utilized. A SiO_2-coated Si wafer (0.4 nm/min) was used as a reference for the sputtering rate. The depth sputter profiling was recorded in five steps at time intervals of 0, 10, 20, 30, and 40 min and quantified in atomic percentage.

The sample treated with diluted solution containing NH_4OH, H_2O_2, and H_2O in a 5:1:4 vol ratio will be referred to as DS-60min, and sample treated with concentrated solution containing NH_4OH and H_2O_2 in a 1:1 vol ratio will be referred to as CS-60min subsequently throughout the study.

2.2. Reactive oxygen species

To assess the generation of hydroxyl radical ($^{\bullet}OH$), the spin trapping technique coupled with electron paramagnetic resonance spectroscopy (EPR) was employed. Cleaned metallic ribbon samples with 0.4 × 1 cm size were immersed in 1 mL of phosphate buffer (PB, 0.5 M, pH 7.4, Sigma-Aldrich, Milan, Italy) containing 0.04 M DMPO (5,5-dimethyl-1-pyrroline-1-oxide, Cayman Chemical Company, Ann Arbor, Michigan) as spin trap molecule, and freshly prepared 0.2 M H_2O_2 as target molecule. The ribbon samples were incubated in the solution at 37 °C, while being continuously stirred using a thermostatic shaker in darkness. After 10, 30, and 60 min, 50 μL of the supernatant were collected in a capillary, and EPR spectra were recorded utilizing a Miniscope MS100 spectrometer (Magnettech, Berlin, Germany) at a microwave power level of 10 mW, a modulation of 1 G, scan range of 120 G, and a center field at 3355 G. A blank control without ribbon samples was prepared. The number of radicals released is proportional to the intensity of the EPR signal. To compare the amount of hydroxyl radicals produced by the ribbon samples, the signals were double integrated using Origin 2023 software and results were reported as arbitrary units. The measurements were conducted in duplicate.

2.3. Measuring biofilm formation

To investigate biofilm formation, model organism for gram-negative *Pseudomonas aeruginosa* (strain PAO1) was utilized [56–58]. The bacterial inoculum was grown in Lysogeny broth (Sigma-Aldrich, LB media: 1 % tryptone, 0.5 % yeast extract, 0.5 % NaCl) in deionized H_2O. Prior to bacterial inoculation, the ribbon samples (0.4 × 2 cm) underwent sterilization by immersion in 70 % ethanol, and each study was conducted with three biological replicates and two technical replicates.

Overnight cultures of *P. aeruginosa* were grown in 15 mL of LB media at 37 °C. Bacteria were quantified by diluting an aliquot 1:10 in fresh media and the optical density (OD) of the bacterial suspension in each tube was measured at 600 nm using a spectrophotometer (Spectramax m384) and adjusted to 0.1 OD (10^7 CFU/mL). The ribbon samples were then incubated without shaking in 1 mL of the bacterial culture for 24 h at 37 °C in sterile 24-well, flat-bottomed, tissue culture-treated plates.

Following the incubation period, the ribbon samples were transferred to a new well-plate containing phosphate-buffered saline (PBS) solution and rinsed gently three times with PBS to remove non-adhered planktonic bacteria. Subsequently, the ribbon samples were dried at 37 °C for 30 min. 1 % crystal violet solution (1 mL) was added to each well and left at room temperature for 15 min. After staining, all the ribbon samples were transferred to a new well-plate and rinsed three times with PBS and dried at 37 °C for 30 min. 1 mL of elution buffer (80 % ethanol and 20 % acetone) was then added to the wells and left at room temperature for 15 min. Afterwards, 1 mL of this elution was transferred to an optically clear plastic cuvette, and the OD of the solution was measured at 595 nm using elution buffer as blank providing a quantitative measurement of biofilm biomass.

2.4. Measuring bacterial adhesion using atomic force microscopy

An overnight culture of *P. aeruginosa* was grown in LB media. Subsequently, 2 mL of the culture was centrifuged in an Eppendorf tube at a speed of 3000 RPM for 15 min, leading to the formation of a visible pellet. The LB media was carefully discarded, and the pellet was resuspended in a 50/50 mixture of PBS and H_2O to prevent osmotic stress. Soft pipetting was employed for resuspension. The mixture was subjected to another round of centrifugation, and the PBS - H_2O combination was discarded. The pellet was completely resuspended in 1 mL of deionized H_2O using soft pipetting.

The optical density (OD) of each Eppendorf tube was measured at 600 nm using a spectrophotometer, with deionized H_2O as blank. Another Eppendorf tube was prepared for each biological replicate, with the OD equalized to 0.1 in deionized H_2O. The required adjustments were made to ensure the uniformity among the ribbon samples.

The metallic ribbon samples before and after treatment were sterilized with 70 % ethanol and allowed to dry in a fume hood. After the drying process, 25 μL of the equalized *P. aeruginosa* (OD: 0.1) culture was added to the top of each sample and spread gently over the surface using a pipette. The ribbon samples were then left to dry for a period of 2–3 h in the fume hood. Once completely dried, the ribbon samples were fixed using a gradient of ethanol washes from 100 % to 50 % and dried under ambient conditions. Cp-Ti and cp-Cu plates were used as control ribbon samples.

Surfaces were imaged before and after inoculation with *P. aeruginosa* using AFM (amplitude modulation atomic force microscopy, MFP-3D, Asylum Research) operated with Si probes (NCH, Nanosensors) having a nominal spring constant of 42 N/m and resonance frequency of 330 kHz. Representative images at 90 x 90 μm, 50 x 50 μm and 10 × 10 μm are shown from images collected in multiple locations. For presentation, images were flattened to remove sample tilt, horizontal correction was applied if required. All ribbon samples are shown with a uniform Z height scale of 400 nm with exception of cp-Cu that has a height of 800 nm due to its complicated topography.

2.5. Metal ion release

Ribbon samples with 0.4 × 0.6 cm size were submerged in cell culture media DMEM (Dulbecco modified eagle medium, Gibco, ThermoFisher scientific) without cells and incubated at a temperature of 37 °C for a period of 3 days to investigate the release of species. Subsequently, 1 mL aliquots of the media were collected for analysis of the released metal species using Agilent ICP-MS, model 7900. The study was conducted with three replicates and normalized against a blank control consisting of cell culture media without any ribbon samples.

2.6. In vitro cytocompatibility analyses

2.6.1. Cell lines and cell culture

The ribbon samples, measuring 0.4 × 0.6 cm, were subjected to sterilization using absolute ethanol for a duration of 5 min. The experiments were conducted in triplicate, employing a 1.5 cm diameter glass coverslip as an internal control for cell growth, from now on referred as “glass control”. Two distinct cell lines were used in this study.

The first cell line, Saos-2 (ATCC), was a transformed cell line of human osteosarcoma tumor cells. These cells were cultured in Dulbecco modified eagle medium (DMEM, Gibco, Thermofisher Scientific) supplemented with 10 % fetal bovine serum (FBS, Gibco, Thermofisher Scientific). Cells were cultured at 37 °C and 5 % CO_2. All the samples

were seeded with a density of 50,000 Saos-2 cells per mL in a 24-well plate.

The second cell line, HOb, was a finite cell line derived from human osteoblasts obtained from a human donor. These cells were cultured in DMEM supplemented with 20 % FBS and maintained at 37 °C with 5 % CO_2. All the samples were seeded with 20,000 HOb cells per mL in a 24-well plate.

2.6.2. Cell viability assay

Cellular cytotoxicity of the samples was assessed on day 3 after seeding using a live/dead kit specifically designed for mammalian cells (Invitrogen). The manufacturer's protocol was followed for staining live cells (green) with calcein and dead cells (red) with ethidium bromide. The stained samples were observed under an inverted fluorescent microscope (Olympus IX71). ImageJ software was utilized for image processing, and the percentage of cell viability was determined by quantifying live and dead cells from four different areas for each sample and replica.

2.6.3. Cell morphology

The morphology of adhered cells on day 3 was analysed using scanning electron microscopy (SEM; Zeiss Merlin, Jena, Germany). The samples were rinsed with PBS, fixed in 4 % paraformaldehyde for 20 min at room temperature, and subsequently rinsed with PBS. Dehydration of the samples was accomplished using an ethanol gradient (50 %, 70 %, 90 %, and 100 %), with each concentration step lasting 10 min. The samples were then dried using hexamethyl-di-silazane for 10 min. Prior to SEM imaging, the samples were sputter-coated with gold and analysed at 2 kx using secondary electron detectors.

2.6.4. Cell adhesion

Cell adhesion on the sample surface was evaluated after 3 days in culture. The actin filaments, representing the cytoskeleton of the cells, were stained using phalloidin. The cells were fixed with 4 % paraformaldehyde for 20 min and washed with PBS, then the samples were immersed in 0.1 % triton for 15 min and 1 % Tween 20 (Sigma) for 20 min at room temperature. Subsequently, the samples were immersed in 1 % PBS-BSA for 20 min at room temperature. A mixture of phalloidin and a nuclei stain consisting of Alexa fluor 594-conjugated phalloidin (Invitrogen), and Hoechst 33258 (Sigma) was used for staining the samples, with an incubation time of 60 min at room temperature. Finally, the samples were washed with PBS and analyzed using a confocal laser scanning microscope (CLSM, Leica SP5). The acquired images were processed using Imaris viewer 9.9.1 software (Oxford Instruments).

2.6.5. Cell proliferation

The metabolic activity of cells growing on the samples was assessed at days 1, 3, and 7 using the Alamar Blue reagent (Thermo Fisher Scientific). At day 1, the samples were transferred to new wells to eliminate background interference from the cells growing at the bottom of the well plate. Subsequently, the samples were incubated in a mixture of cell media and Alamar Blue reagent (dilution of 10:1) for 4 h in the dark at 37 °C with 5 % CO_2. A negative control of Alamar Blue without any sample was prepared as a standard reference. Following the incubation period, the supernatant was collected, and the fluorescence intensity was measured at an excitation wavelength of 560 nm and an emission wavelength of 585 nm using a spark multimode microplate reader (Tecan, Männedorf, Switzerland). Fresh cell culture medium was added after the assay and the experiment was repeated on day 3 and 7.

2.6.6. Cell differentiation

The differentiation of cells was investigated by assessing alkaline phosphatase (ALP) activity at 7 and 14 days of incubation. The cells incubated on the samples for the specified durations were lysed in CyQuant cell lysis buffer (Thermo Fisher Scientific). Lysis was achieved by transferring the samples to eppendorf tubes and subjecting them to 10 min of lysis, followed by 10 sec of vortexing. Subsequently, the cell lysates were centrifuged at 12,000 rpm for 4 min at 4 °C, and the resulting supernatants were collected. ALP activity was measured by employing the hydrolysis of p-nitrophenyl phosphate (pNPP), resulting in the production of p-nitrophenol (pNP). Specifically, 25 μL of 1-step pNPP (Thermo Fisher Scientific) was mixed with 25 μL of the collected supernatant. The absorbance at 405 nm was measured using a Nanodrop Spectrophotometer (Thermo Fisher Scientific).

2.7. Statistical analysis

The data are presented using mean ± standard error of the mean (SEM). In case of normally distributed data, ordinary one-way ANOVA followed by Dunnett's or Tukey's post hoc test was used. A 95 % confidence interval was applied, and values with $P < 0.05$ were considered statistically significant, unless otherwise stated. GraphPad Prism 8.0.2 software was used for conducting statistical analysis.

3. Results and discussion

3.1. Sample preparation and characterization

The structure and thermal properties of the as-quenched ribbon were analyzed using XRD and DSC, as shown in Figure S1. The DSC plot reveals good glass-forming ability (GFA) of the alloy with two crystallization peaks, onset temperatures Tx1 at 422.5 °C and Tx2 at 509.0 °C, and a glass transition temperature (Tg) at 382.0 °C. The XRD pattern exhibits a broad halo, confirming the formation of a completely amorphous ribbon [55]. FESEM analysis of the DS-60min treated ribbon samples in Fig. 1a and Figure S 2 a, shows a homogeneously distributed nanostructure with interconnected ligaments. In contrast, the CS-60min sample in Fig. 1b and Figure S 2 b exhibits a bimodal pore distribution and interconnected ligaments. Both treated surfaces demonstrate hydrophilic behavior, with contact angles of 64.1 ± 4.8° for DS-60min and 68.8 ± 6.3° for CS-60min, compared to 75.1 ± 3.6° for the untreated ribbon. The XPS sputter depth profile data (Table 1) indicate that the treated surface is mainly composed by mixed Ti/Zr oxides in which the overall Cu content is drastically reduced with respect to the as quenched sample, apart from an enrichment in Cu content in the outermost region possibly due to a reprecipitation process during chemical treatment. The other minor constituents (Fe, Sn, Ag) remained in low concentration on the sample surface.

3.2. Reactive oxygen species

Hydroxyl radical release was quantified in a cell-free system simulating the inflammatory environment within the human body. The DS-60min ribbon samples exhibited greater reactivity in hydroxyl radical release after 10 min of incubation compared to the other samples (Fig. 2). Reactivity further increased at 30 and 60 min of incubation. Similarly, the CS-60min ribbon samples demonstrated the ability to release hydroxyl radicals, which was significantly higher than the untreated ribbon sample. The observed trend in hydroxyl radical generation by the ribbon samples corresponds to the release of Cu ions ($Cu^{+/2+}$) from the sample surface, suggesting the involvement of Cu ions in the mechanism of hydroxyl radical generation. It is worth to note that the chemical mechanism of the radical generation involves copper ions ($Cu^{+/2+}$) in solution, hence after solubilization from the alloy has occurred. In this case, Cu ions are recognized for generating reactive hydroxyl species in a Fenton-type reaction, as depicted in the reaction 1 [59,60]. The concentration of Cu atoms of 14.1 % on the sample surface is determined from XPS results (Table 1) and its concentration drastically decreases in the inner oxide layer regions, with Ti and Zr becoming dominant. We can infer that the major contribution to the release of Cu ions is related to the high concentration of this element on the sample

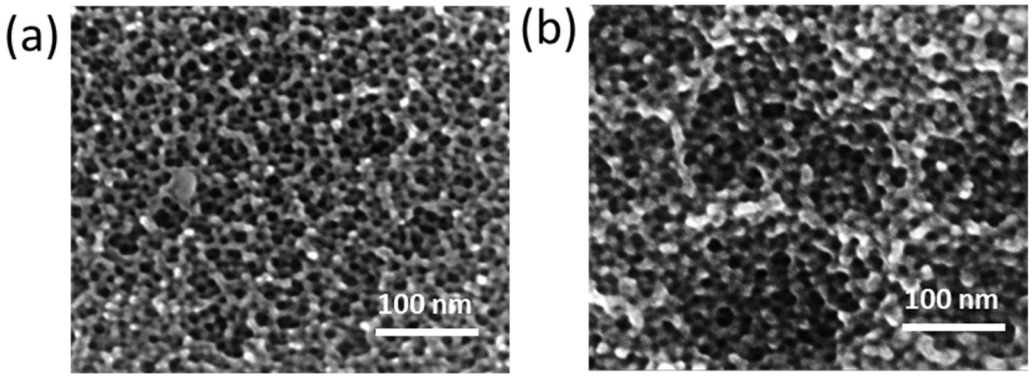


Fig. 1. FESEM micrographs of DS sample (NH_4OH, H_2O_2, and H_2O in a 5:1:4 vol ratio) and CS sample (NH_4OH, H_2O_2, in a 1:1 vol ratio), (a) DS-60min sample, (b) CS-60min sample at 500kx.

Table 1
XPS sputter depth profile of DS-60min sample.

	Element content (at%)						
Depth (nm)	O	Ti	Cu	Zr	Fe	Sn	Ag
0	64.0	10.9	14.1	6.8	0.8	2.2	1.0
4	57.0	19	10.0	9.7	1.4	1.5	1.2
8	57.9	20.2	5.7	11.8	2.1	0.9	1.3
12	51.5	22.6	7.9	12.2	2.0	1.2	2.4
16	31.6	29.2	19.3	12.6	1.8	3.1	2.3

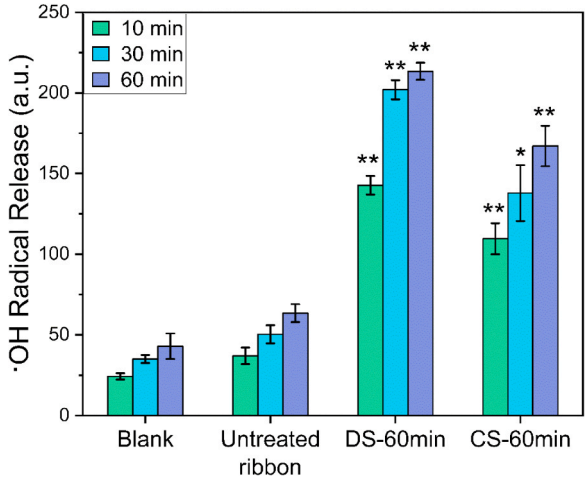


Fig. 2. DMPO-OH adduct concentration measured by double integration of EPR spectra of ribbon samples after 10, 30, 60 min of incubation. Data represented with mean ± SEM of three independent experiments and analyzed using ordinary one-way ANOVA, followed by Dunnett's post-hoc test. *P < 0.05, **P < 0.01 (treated vs untreated ribbons).

surface and not to the surface morphology that it is not drastically affecting the surface area of the sample. The transition in composition from the surface to the bulk of the sample could influence the release of $Cu^{+/2+}$ ions which produce ROS and presence of Ti oxide species can additionally contribute to the generation of hydroxyl radical species. The emission of $^{\bullet}OH$ in the absence of light may be attributed to the binding of H_2O_2 on the Ti(IV) surface, resulting in the formation of hydroperoxyl radicals (>Ti III–$^{\bullet}OOH$) through an inner-sphere electron transfer mechanism. The hydroperoxyl radicals generated on the surface can undergo additional decomposition to generate $^{\bullet}OH$ radicals (reaction 2) [61–64]. The oxidative stress associated to the material surface represents an indication of the surface reactivity of the material. This type of assessment is usually performed in short timing after incubation in fluids due to the rapid decay of the radical species formed and saturation of the effect [65–69].

$$Cu^{+} + H_2O_2 \rightarrow Cu^{2+} + OH^{-} + {}^{\bullet}OH \quad (1)$$

$$Ti^{4+}{-}OOH \leftrightarrow Ti^{3+}{-}{}^{\bullet}OOH \quad (2)$$

3.3. Biofilm formation and bacterial adhesion study with Pseudomonas aeruginosa (PAO1)

To measure biofilm formation, 1 % crystal violet was used to stain the biomass adhered to the surface of the samples. As crystal violet binds non-specifically to cells and extracellular polymeric substances, it allows us to conduct a quantification of the biofilm biomass. The results showed that, when *P. aeruginosa* biofilms are grown in contact with the different groups for 24 h, it is possible to observe a significant difference between the untreated ribbons, DS-60min and CS-60min ribbon samples in comparison to cp-Ti, which suggests that the ribbons possess an anti-biofilm effect as it can reduce biofilm formation (Fig. 3). The DS-60min proved to be as effective as cp-Cu, followed by the CS-60min and the untreated ribbon.

The samples were also analyzed qualitatively by AFM to identify bacterial adherence, coverage, and bacterial surface behavior in contact with these surfaces. On Fig. 4, it is possible to visualize the samples before inoculation (topographical analysis) and after inoculation

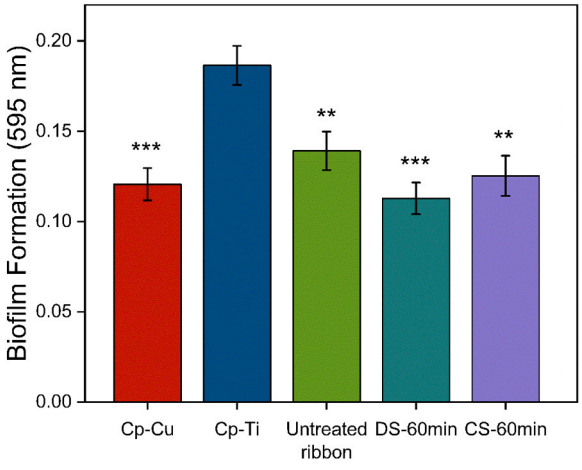


Fig. 3. Biofilm formation study by *P. aeruginosa* analyzed using 1 % crystal violet assay after 24 h incubation. Data represented with mean ± SEM of three independent experiments and analyzed using ordinary one-way ANOVA, followed by Dunnett's post hoc test. **P < 0.01, ***P < 0.001 (vs cp-Ti).

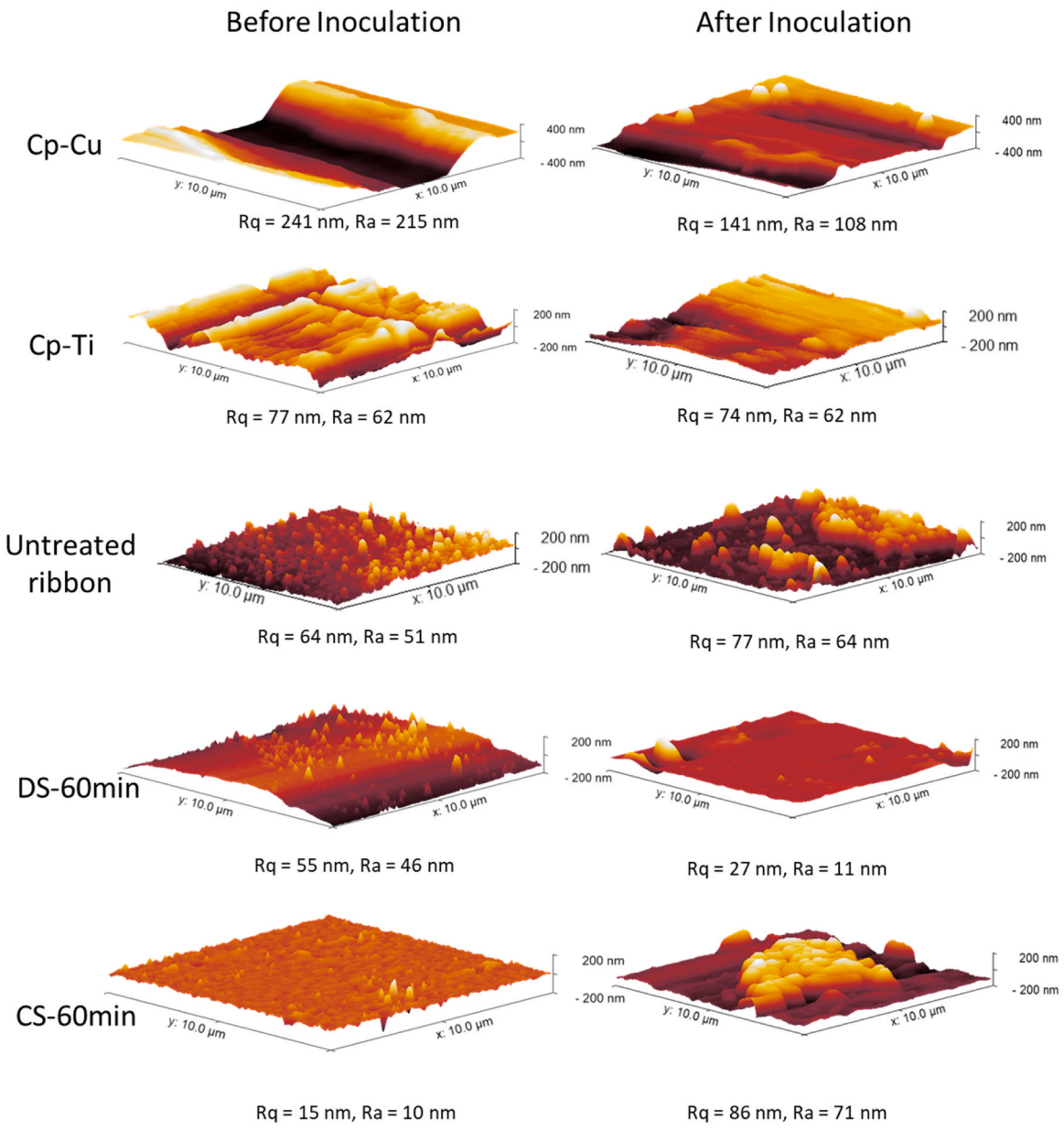


Fig. 4. 3D topographical and biological AFM qualitative analysis 10 x10 µm images before and after inoculation with *P. aeruginosa* (PA01) for 2 h. The height data scale was uniform for all samples at 400 nm except for cp-Cu with 800 nm. All samples were analyzed using the software Gwyddion.

(biological analysis) in 3D view. The average roughness (Ra) and root mean square roughness (Rq) was calculated for each sample and presented below each image for comparison between analyses. Decreased adherent and planktonic bacteria prevalence were significantively seen after 2 h when *P. aeruginosa* came into contact with cp-Cu and DS-60min as confirmed by the decrease of roughness in the surface. While on the untreated and CS-60min ribbon samples it was possible to appreciate an agglomeration of bacteria suggesting early-biofilm formation. On CS-60min it was possible to differentiate each cell from the cluster alongside an increase of the roughness confirming bacterial presence. Simultaneously on the untreated ribbon there is a slight increase in roughness, alongside agglomerated bacteria that are not easily visualized individually after 2 h.

The distinct antibiofilm properties observed between DS-60min and CS-60min can be attributed to a combined effect due to variations in their surface topography, wettability, and ability to release Cu species. According to force-distance curve proposed by Cheng et al. [70] textured surfaces with small pore sizes significantly reduce bacterial attachment due to weaker interactions and higher energy barriers preventing adhesion as in the case of DS-60min sample. Moreover, the hydrophilicity associated with DS-60min sample inhibits bacterial adhesion through hydrogen bonding and ionic interactions with surrounding liquid where "conditioning film" with adsorbed molecules are formed. In literature it was reported that effective bactericidal response was observed on nanostructured Ti surfaces with hydrophilicity 71°, due to cell membrane deformation of *P. aeruginosa* at the initial attachment on to the surface [71]. In contrast, CS-60min has bimodal porosity in which the larger pores (178.6 ± 44.6 nm) can reduce energy barriers for bacteria, enhancing adhesion, while the smaller nanostructures on the surface contribute to a certain level of anti-adhesion and could reduce bacterial attachment [72]. The combination of these factors makes CS-60min less effective in preventing *P. aeruginosa* adhesion and biofilm formation compared to DS-60min.

3.4. Metal ion release

Metal ion release from the ribbon samples was assessed using ICP-MS to explore potential leaching from the sample surface. The ribbon samples were immersed in DMEM cell culture media for 3 days at 37 °C, and the measured species released in the cell culture media are depicted in Fig. 5. A notable difference is evident, with DS-60min exhibiting the highest release of Cu ions, followed by CS-60min and the untreated ribbon sample, which displays limited release. The release of Cu ions ($Cu^{+/2+}$) in the DMEM media can be ascribed to the existence of Cu atoms predominantly present in the outer region of the nanoporous layer on the treated sample. The XPS sputter depth profile of DS-60min supports this observation, revealing that Cu atoms remains detectable in the outermost oxide layer regions subsequently impacting the release of Cu ions into the surrounding media. Even if other elements were detected on the sample surface by XPS (Table 1), it is possible that their release is very limited, so that their amount results to be below the detection limit of ICP-MS, and any engagement in ROS catalytic activity or direct damage to cells/bacteria was excluded.

The different chemistry and morphology affect both cytocompatibility and antibacterial activity via different possible actions. (i) Cu release: Cu can be a cytotoxic element but when released in a limited amount can kill bacteria by ROS production via Fenton reaction. (ii) Morphology: cells and bacteria participate in the race for the surface to adhere on the implanted materials, roughness and wettability of the surface can play a major role to favor cell with respect to bacteria.

Several studies have reported Cu as a cytotoxic element [73–75]. However, when Cu is alloyed with biocompatible elements such as Ti and Zr it does not show cytotoxic behavior [76]. Pd based dental alloys with composition $Pd_{80}Cu_{10}Ga_{10}$ wt% showed a Cu release in cell cultured media between 0.1 mg/L and 1 mg/L and the cell viability with mouse fibroblast cells was 81 ± 8 % and 75 ± 13 %, respectively. However, when the Cu ion release increased at 10 mg/L the cell viability was reduced to 54 ± 16 % [77]. Chai et al. [78] reported an in vitro response of bacteria (*S. aureus and E. coli*) and cells (MG63 osteoblast-like cells) on bone screws made from austenitic stainless steel with 4.5 wt% Cu (317L–Cu). The reported Cu ion concentration in the rabbit blood after 72 h of incubation was approximately 1 mg/L and the 317L–Cu sample shows good biocompatibility, no evident toxicity with MG63 osteoblast-like cells and good antimicrobial activity as compared with Ti6Al4V control alloy. The in vivo study indicated that 317L- Cu can stimulate osteoblast like cell growth and significantly reduce infection and inflammation in rabbits. Moreover, Cu is known for killing bacteria by various routes, one possible is by ROS via Fenton reaction which induces cellular stress and impact bacterial membrane integrity of bacteria [79,80].

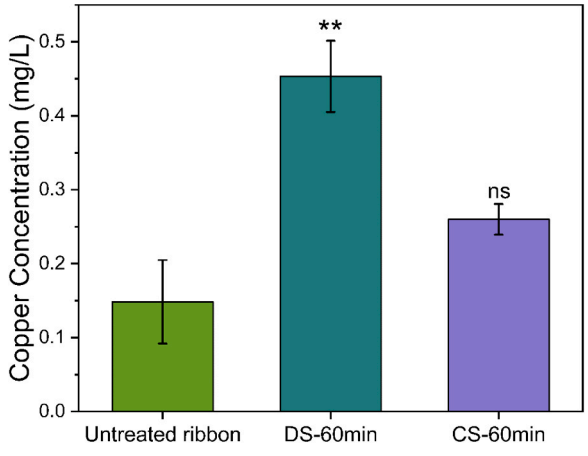


Fig. 5. ICP-MS measurement of Cu species release in cell culture media without cells after 3 days of incubation. Data represented with mean ± SEM of three independent experiments and analyzed using ordinary one-way ANOVA, followed by Dunnett's post-hoc test. **P < 0.01 (treated vs untreated ribbons).

3.5. Cytocompatibility assessment with Saos-2 and HOb cells

In the case of the treated sample DS-60min and CS-60min, it is observed that the surfaces showed significantly high concentration of Cu species released in the cell culture media. Therefore, it is important to determine the tolerance limit of the treated surfaces by investigating the cytocompatibility of the sample to obtain a balanced activity as an implant material.

The cytocompatibility of the samples were investigated using two cell lines i.e., Saos-2 and HOb. The cytocompatibility studies included cell viability test using live/dead kit after 3 days in culture, cell morphology and adhesion after 3 days, cell proliferation after 1, 3, and 7 days, and cell differentiation studies involving ALP activity after 7 and 14 days.

On day 3 after cell seeding, the cytotoxicity of the samples was analyzed using live/dead kit. Live cells were stained green and dead cells were stained red via calcein and ethidium bromide staining, respectively. The result showed abundance of live cells, while only a few dead cells were observed on the surface of DS-60min and CS-60min sample (Fig. 6). For Saos-2 cells, rounded cells were observed on the DS-60min and CS-60min sample. However, for HOb cells, the samples showed well spread cells on the surface after 3 days in culture. The cell viability of samples was above 98 % and 96 % for Saos-2 and HOb cells, respectively. In addition, the number of adhered live cells on the sample surface were quantified (Table 2). We observed that the untreated ribbon presented the highest number of Saos-2 cells, followed by the DS-60min, glass control and the CS-60min samples. For instance, the number of HOb cells was higher on DS-60min than on CS-60min and glass control, being the untreated ribbon the sample with less cells. It is noteworthy to acknowledge that HOb cells, being larger in size than Saos-2 cells, resulted in comparatively lower cell counts across all tested samples.

As stated, the morphology of the adhered cells on the samples was analyzed using SEM (Fig. 7). Saos-2 cells grown over the untreated ribbon samples showed flat cells after 3 days in culture. However, over DS-60min sample some cells presented a more rounded morphology, along with some flat well adhered cells (shown in the inset) with polygonal morphologies and filipodia spread on the surface. In CS-60min sample, flat cells were observed with polygonal morphology with contacts between cells, although few rounded cells were also observed in the vicinity of the flat cells (shown in the inset). The presence of rounded cells could indicate some degree of cell death. In few cases, the morphology was compatible with apoptosis, a type of regulated cell death [81–83]. These results could be due to surface chemistry of the DS-60min and CS-60min ribbon samples which show presence of Cu species on the near surface region of the *pseudo-dealloyed* sample. On the other hand, HOb cells cultured on all samples were flat and well spread on the surface of all samples. Prolonged filopodia extensions were observed on all the samples which indicate presence of healthy cells with visible nucleus and nucleoli within the nucleus. Interestingly, the presence of rounded Saos-2 cells previously observed on DS-60min and CS-60min ribbon samples was not observed for HOb cells. Both cell lines are osteoblasts, but from different origins. Saos-2 cells are tumoral cells, whereas HObs are cells isolated from healthy patients. In this regard, the results showed a different behavior when cultured on the same surface type.

Adhesion was studied through the analysis of stress fibers via the actin filaments staining of Saos-2 and HOb cells (Fig. 8). The cells grown on all sample surfaces showed well defined actin stress fibers after 3 days of incubation. This indicates that cells were able to adhere and spread to the surface of the samples. The multidirectional distribution of the actin filaments could be due to surface topography of the sample. The actin filaments can be seen aligning at one end forming contact points between cells to cells or cells to substrate. For Saos-2 cells, few cells

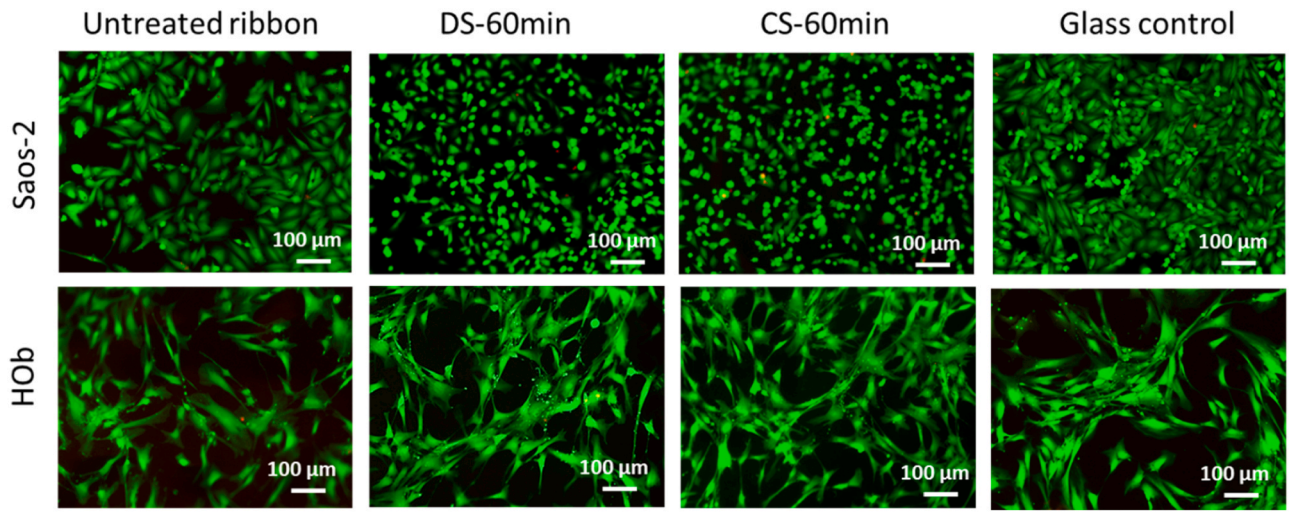


Fig. 6. Cytotoxicity measurements using live/dead kit measured on Saos-2 and HOb cells after 3 days of incubation. Live cells represented in green and dead cells in red.

Table 2
The number of adhered Saos-2 and HOb cells on the samples.

Samples	Saos-2 cells/cm^2	HOb cells/cm^2
untreated ribbon	63146 ± 6479	10423 ± 2170
DS−60min	53913 ± 5690	14190 ± 3678
CS−60min	39550 ± 4498	13660 ± 6256
glass control	46466 ± 10070	13194 ± 2244

showed short and disrupted actin bundles which corresponds to less spread cells or rounded cells growing on DS-60min and CS-60min ribbon samples. These results are in agreement with the ones observed for morphology using SEM.

Furthermore, Saos-2 and HOb cell proliferation was analyzed after 1, 3, 7 days in culture (Fig. 9a, b). The results showed no significant differences on Saos-2 neither on HOb cell proliferation among untreated ribbon, DS-60min and CS-60min ribbon samples over time. The gradual increase in the cell proliferation between 3 and 7 days indicates that both cell lines were able to adhere to the sample surface and to proliferate. By contrast, significant differences were found in cell proliferation between the three ribbon samples (untreated ribbon, DS-60min and CS-60min) and the glass control samples. Denoting that, at least, during the first days on culture, the metabolic activity is higher for both type of cells growing on glass control surfaces, even though no cytotoxicity was detected. Nevertheless, the rate of proliferation from day 3 to day 7 is similar among all samples and control (approximately 2.5) for Saos-2 cells and no significant differences were found for HOb cells.

Finally, the samples were investigated for cell differentiation by measuring ALP enzyme activity of Saos-2 cells after 7 and 14 days in culture (Fig. 9c) and HOb cells after 14 days (Fig. 9d). The ALP activity of Saos-2 cells growing on samples was already detected after 7 days in culture, and the activity was maintained after 14 days in culture. No significant difference between the ribbon samples and glass control was observed for both time points evaluated. For HOb cells, ALP activity of cells growing on the three ribbon samples was detected, although the activity was lower compared to Saos-2 cells. Similar ALP activity was observed among the ribbon samples and significant differences were observed when comparing the ribbon samples with glass control.

Saos-2 and HOb cells showed different behavior when cultured on the same samples. Saos-2 cells proliferated faster than HOb cells, although for each cell line no significant differences were observed among samples. Similarly, Saos-2 cells showed higher ALP activity compared to HOb cells. It is known that tumor cells have rapid proliferation, and the contact inhibition is disrupted [84]. In this sense,

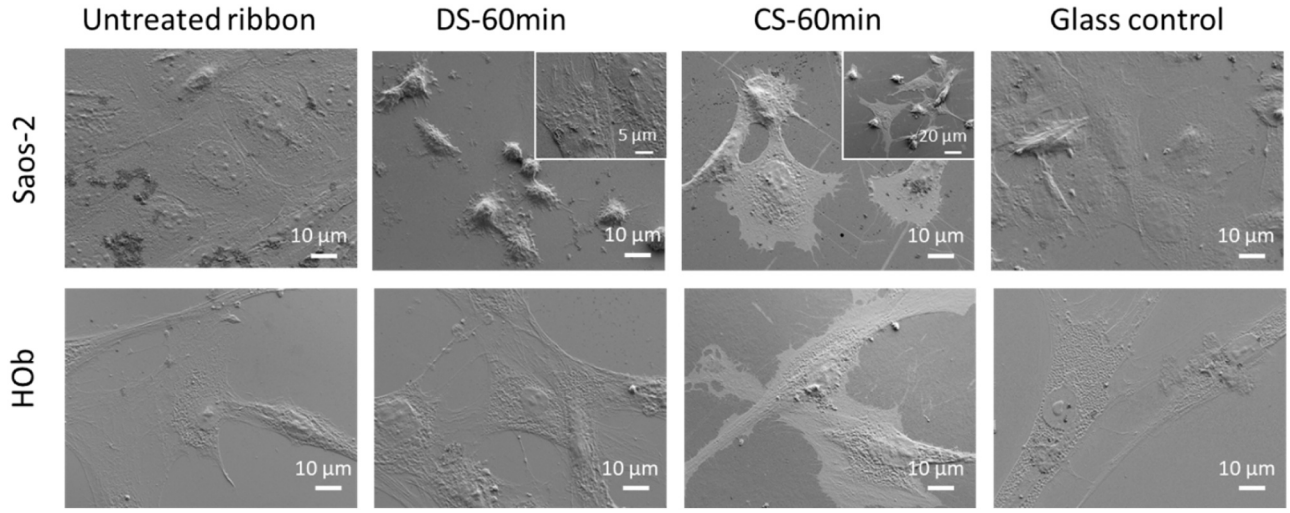


Fig. 7. SEM micrographs of Saos-2 and HOb cells on sample surfaces after 3 days of incubation.

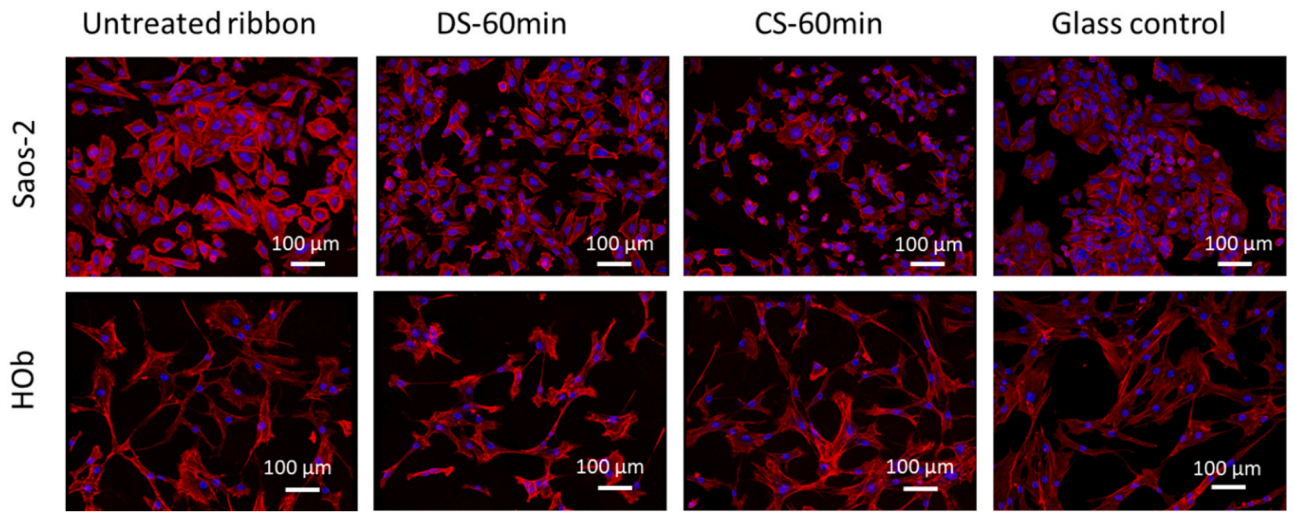


Fig. 8. CLSM images of samples with Saos-2 and HOb cells after 3 days of incubation. Stress fibers (actin; red) and nuclei (DNA; blue).

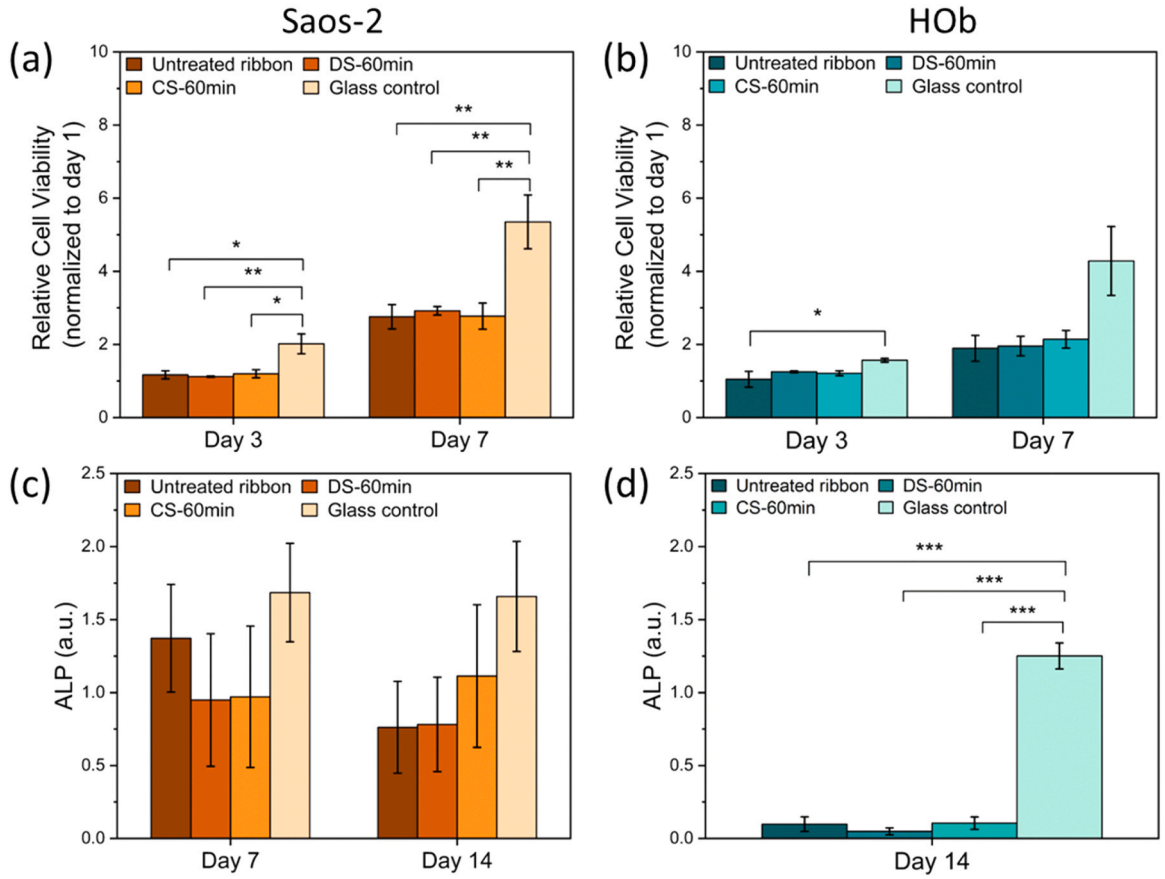


Fig. 9. Cell proliferation was measured using Alamar Blue assay for 3 days of incubation of (a) Saos-2 cells and (b) HOb cells. ALP activity measured after 7 and 14 days of incubation for (c) Saos-2 cells and after 14 days of incubation for (b) HOb cells. Data represented with mean ± SEM of three independent experiments and analyzed using ordinary one ANOVA, followed by Tukey's post hoc test for multiple comparisons. *P < 0.05, **P < 0.01, ***P < 0.001.

several authors have considered that HOb cells from healthy donors are cells that mimic better the in vivo cellular processes [85]. Regarding osteoblasts differentiation, a comparison between Saos-2 and HOb cells was previously performed by other authors, and the results demonstrated that both cell lines had similar differentiation pattern [85]. However, HOb cells are usually cultured using a differentiation cell culture medium that contains differentiation supplements. In the present paper, the use of differentiation supplements was avoided to evaluate the effect of the ribbon samples and the sample surfaces topography on osteoblasts differentiation. Thus, the ALP activity of HOb cells was due to the spontaneous differentiation that occurred over time. For Saos-2 cells, their more mature phenotype due to tumoral origin was responsible for the higher initial levels of ALP activity.

4. Summary of key findings and conclusion

The goal of this study was to design the surface morphology and composition of Ti-based amorphous alloys to achieve enhanced biocompatibility and antibacterial activity. A novel and facile chemical treatment process was applied to create patterned Ti/Zr mixed oxide surfaces with two samples, DS-60min and CS-60min, produced using NH_4OH and H_2O_2 solutions in different ratios (DS-60min: NH_4OH, H_2O_2, and H_2O in a 5:1:4 vol ratio; CS-60min: NH_4OH and H_2O_2 in a 1:1 vol ratio). These samples exhibited distinct chemical and morphological characteristics, including differences in nanoporous topography, wettability, and Cu release, which significantly influenced their cytocompatibility and antibacterial performance. The DS-60min sample had a nanoporous topography with ligaments of 10.7 ± 1.3 nm thickness, pores of 11.4 ± 1.6 nm, wettability of 64°, and Cu ion release of 0.45 ± 0.04 mg/L, while the CS-60min sample featured a bimodal porosity with smaller pores (15.3 ± 4.6 nm), larger pores (178.6 ± 44.6 nm), ligaments of 12.4 ± 3.1 nm, wettability of 68.8°, and lower Cu ion release of 0.26 ± 0.02 mg/L. The different chemistries and morphologies influenced cytocompatibility and antibacterial activity through varied mechanisms. The Cu released in limited amounts contributed to antimicrobial effects via ROS production through the Fenton reaction, and surface morphology played a pivotal role in influencing the "race for the surface" by favoring cell adhesion over bacterial adhesion. Literature indicates that while Cu can be cytotoxic in high concentrations, its controlled release (e.g., 0.1–1 mg/L) in alloys with biocompatible elements ensures good antibacterial efficacy while maintaining cytocompatibility. In this study, Cu release levels for both DS-60min and CS-60min were within the safe range and supported cell viability while reducing biofilm formation. The DS-60min sample exhibited significantly reduced biofilm formation, comparable to cp-Cu in crystal violet assays, and AFM analysis confirmed reduced bacterial adhesion and planktonic bacteria. In contrast, CS-60min samples showed early biofilm formation due to their bimodal porosity, where larger pores lowered the energy barrier for bacterial attachment. The DS-60min sample's unimodal small pore size and hydrophilic surface enhanced bacterial resistance, likely due to increased energy barriers for adhesion and the inhibitory role of hydrogen bonding with surrounding liquid molecules. Furthermore, ROS production and Cu ion release for DS-60min were higher than CS-60min, contributing to its superior antibiofilm properties, while both samples exhibited significant biocompatibility with Saos-2 and HOb cells, showing no cytotoxicity and supporting cell proliferation and early osteogenic differentiation. However, while the study demonstrated promising antibacterial efficacy, particularly against gram-negative *P. aeruginosa*, broader studies involving gram-positive and drug-resistant bacteria are required to assess the potential for a broad-spectrum antibacterial effect. The DS-60min sample, with its hierarchically structured nanoporous surface and residual Cu, balances biofilm resistance and cytocompatibility in the "race for the surface," offering significant potential for medical implant applications.

Funding information

This work has received funding from the European Union's Horizon 2020 research and innovation programme under the Marie Skłodowska-Curie grant agreement No. 861046 (Bioremia European Training Networks), grant PID2020 116844RB-C22 funded by MCIN and 2021-SGR-00122 funded by the Generalitat de Catalunya. Funding from a postdoctoral fellowship within the Beatriu de Pinós programme, funded by the Secretary of Universities and Research (Government of Catalonia) and by the Horizon 2020 programme of research and innovation of the European Union under Marie Sklodowska-Curie grant agreement No. 801370. Authors acknowledge support from Project CH4.0 under the MUR program "Dipartimenti di Eccellenza 2023–2027" (CUP: D13C22003520001). Deutsche Forschungsgemeinschaft (DFG) under the grant agreement No. 458057521; GE 1106/15–1 for the financial support.

CRediT authorship contribution statement

Nora Fernandez Navas: Writing – review & editing. **Federico Scaglione:** Investigation. **Brian Rodriguez:** Writing – review & editing, Formal analysis. **Annett Gebert:** Writing – review & editing, Resources, Funding acquisition. **Francesco Turci:** Writing – review & editing, Resources, Funding acquisition. **Tadhg Ó Cróinín:** Writing – review & editing, Resources, Funding acquisition. **Carme Nogués:** Writing – review & editing, Resources, Funding acquisition. **Kirti Tiwari:** Writing – original draft, Visualization, Validation, Methodology, Investigation, Formal analysis, Conceptualization. **Paola Rizzi:** Writing – review & editing, Visualization, Validation, Supervision, Resources, Project administration, Funding acquisition, Conceptualization. **Andreu Blanquer:** Writing – review & editing, Validation, Methodology, Investigation, Formal analysis. **David Zermeño Pérez:** Writing – review & editing, Validation, Methodology, Investigation, Formal analysis. **Cristina Pavan:** Writing – review & editing, Validation, Methodology, Investigation. **Maura Tomatis:** Writing – review & editing, Validation, Methodology.

Declaration of Competing Interest

The authors declare that they have no known competing financial interests or personal relationships that could have appeared to influence the work reported in this paper.

Acknowledgment

The authors would like to thank the staff from the Servei de Microscòpia of Universitat Autònoma de Barcelona and Martin Hantusch from Leibniz-IFW Dresden for XPS analysis.

Appendix A. Supporting information

Supplementary data associated with this article can be found in the online version at doi:10.1016/j.jallcom.2025.178584.

Data availability

Data will be made available on request.

References

[1] M. Geetha, A.K. Singh, R. Asokamani, A.K. Gogia, Ti based biomaterials, the ultimate choice for orthopaedic implants - A review, Prog. Mater. Sci. 54 (2009) 397–425, https://doi.org/10.1016/j.pmatsci.2008.06.004.
[2] M. Sarraf, E. Rezvani Ghomi, S. Alipour, S. Ramakrishna, N. Liana Sukiman, A state-of-the-art review of the fabrication and characteristics of titanium and its alloys for biomedical applications, Bio-Des. Manuf. 2021 5:2 5 (2021) 371–395, https://doi.org/10.1007/S42242-021-00170-3.
[3] V.K. Manivasagam, K.C. Popat, Hydrothermally treated titanium surfaces for enhanced osteogenic differentiation of adipose derived stem cells, Mater. Sci. Eng.: C. 128 (2021) 112315, https://doi.org/10.1016/J.MSEC.2021.112315.
[4] J. Vishnu, V. K Manivasagam, V. Gopal, C. Bartomeu Garcia, P. Hameed, G. Manivasagam, T.J. Webster, Hydrothermal treatment of etched titanium: a potential surface nano-modification technique for enhanced biocompatibility, Nanomedicine 20 (2019) 102016, https://doi.org/10.1016/J.NANO.2019.102016.
[5] G. Manivasagam, D. Dhinasekaran, A. Rajamanickam, Biomedical implants: corrosion and its prevention-A review, Recent Pat. Corros. Sci. 2 (2010) 40–54.
[6] L.-C. Zhang, L.-Y. Chen, A review on biomedical titanium alloys: recent progress and prospect, Adv. Eng. Mater. 21 (2019) 1801215, https://doi.org/10.1002/ADEM.201801215.
[7] Z.A. Uwais, M.A. Hussein, M.A. Samad, N. Al-Aqeeli, Surface modification of metallic biomaterials for better tribological properties: a review, Arab J. Sci. Eng. 42 (2017) 4493–4512, https://doi.org/10.1007/S13369-017-2624-X/METRICS.
[8] V.K. Manivasagam, R.M. Sabino, P. Kantam, K.C. Popat, Surface modification strategies to improve titanium hemocompatibility: a comprehensive review, Mater. Adv. 2 (2021) 5824–5842, https://doi.org/10.1039/d1ma00367d.

[9] I. Francolini, G. Donelli, Prevention and control of biofilm-based medical-device-related infections, FEMS Immunol. Med. Microbiol. 59 (2010) 227–238, https://doi.org/10.1111/j.1574-695X.2010.00665.x.

[10] V.K. Manivasagam, M. Sankar, Caterina, B. Garcia, J. Vishnu, Kaushik Chatterjee, Satyam Suwas, G. Manivasagam, Thomas, J. Webster, C.B. Garcia, K. Chatterjee, S. Suwas, T.J. Webster, Surface-modified WE43 magnesium alloys for reduced degradation and superior biocompatibility, Vitr. Models 2022 1:3 1 (2022) 273–288, https://doi.org/10.1007/S44164-022-00016-X.

[11] R.D. Scott, The Direct medical costs of healthcare-associated infections in U.S. hospitals and the benefits of prevention, (2009). ⟨https://stacks.cdc.gov/view/cdc/11550⟩ (accessed November 29, 2023).

[12] P.W. Stone, Economic burden of healthcare-associated infections: an American perspective, Expert Rev. Pharm. Outcomes Res 9 (2009) 417, https://doi.org/10.1586/ERP.09.53.

[13] D. Almasri, Y. Dahman, S. Fiorilli, D. Almasri, Y. Dahman, Prosthetic joint infections: biofilm formation, management, and the potential of mesoporous bioactive glass as a new treatment option, Pharmaceutics 2023 15 (15) (2023) 1401, https://doi.org/10.3390/PHARMACEUTICS15051401.

[14] J. Schroers, G. Kumar, T.M. Hodges, S. Chan, T.R. Kyriakides, Bulk metallic glasses for biomedical applications, JOM 61 (2009) 21–29, https://doi.org/10.1007/S11837-009-0128-1/METRICS.

[15] W.L. Johnson, Bulk glass-forming metallic alloys: science and technology, MRS Bull. 24 (1999) 42–56, https://doi.org/10.1557/S0883769400053252.

[16] M. Miller, P. Liaw, Bulk. Met. Glass.: Overv. (2008), https://doi.org/10.1007/978-0-387-48921-6.

[17] M. Chen, A brief overview of bulk metallic glasses, NPG Asia Mater. 2011 3:9 3 (2011) 82–90, https://doi.org/10.1038/asiamat.2011.30.

[18] W. Yang, Y. Liu, N. Hua, S. Pang, Y. Li, P.K. Liaw, T. Zhang, Formation and properties of biocompatible Ti-based bulk metallic glasses in the Ti – Cu – Zr – Fe – Sn – Si – Ag system, J Non Cryst Solids 571 (2021) 121060, https://doi.org/10.1016/j.jnoncrysol.2021.121060.

[19] H. Yan, Y. Liu, S. Pang, Glass formation and properties of Ti-based bulk metallic glasses as potential biomaterials with Nb additions, Rare Met. 37 (2018) 831–837, https://doi.org/10.1007/s12598-015-0664-5.

[20] C. Wang, N. Hua, Z. Liao, W.E.I. Yang, S. Pang, P.K. Liaw, T.A.O. Zhang, Ti-Cu-Zr-Fe-Sn-Si-Ag-Pd bulk metallic glasses with potential for biomedical applications, Metall. Mater. Trans. A 52 (2021) 1559–1567, https://doi.org/10.1007/s11661-021-06183-y.

[21] Y. Liu, S. Pang, H. Li, Q. Hu, B. Chen, T. Zhang, Formation and properties of Ti-based Ti-Zr-Cu-Fe-Sn-Si bulk metallic glasses with different (Ti + Zr)/Cu ratios for biomedical application, Intermetallics (Barking) 72 (2016) 36–43, https://doi.org/10.1016/j.intermet.2016.01.007.

[22] S. Hasani, P. Rezaei-Shahreza, A. Seifoddini, M. Hakimi, Enhanced glass forming ability, mechanical, and magnetic properties of Fe41Co7Cr15Mo14Y2C15B6 bulk metallic glass with minor addition of Cu, J. Non Cryst. Solids 497 (2018) 40–47, https://doi.org/10.1016/J.JNONCRYSOL.2018.05.021.

[23] M. Shi, R. Li, J. Wang, Z. Liu, X. Luo, T. Zhang, Effects of minor Cu addition on glass-forming ability and magnetic properties of FePCBCu alloys with high saturation magnetization, Philos. Mag. 93 (2013) 2182–2189, https://doi.org/10.1080/14786435.2013.765986.

[24] C.H. Lin, C.H. Chen, Y.S. Huang, C.H. Huang, J.C. Huang, J.S.C. Jang, Y.S. Lin, In-vivo investigations and cytotoxicity tests on Ti/Zr-based metallic glasses with various Cu contents, Mater. Sci. Eng.: C. 77 (2017) 308–317, https://doi.org/10.1016/J.MSEC.2017.03.228.

[25] M. Biały, M. Hasiak, A. Łaszcz, Review on biocompatibility and prospect biomedical applications of novel functional metallic glasses, J. Funct. Biomater. 2022 13 (13) (2022) 245, https://doi.org/10.3390/JFB13040245.

[26] T. Xue, S. Attarilar, S. Liu, J. Liu, X. Song, L. Li, B. Zhao, Y. Tang, Surface modification techniques of titanium and its alloys to functionally optimize their biomedical properties: thematic review, Front. Bioeng. Biotechnol. 8 (2020) 603072, https://doi.org/10.3389/FBIOE.2020.603072/BIBTEX.

[27] V.K. Manivasagam, K.C. Popat, In vitro investigation of hemocompatibility of hydrothermally treated titanium and titanium alloy surfaces, ACS Omega 5 (2020) 8108–8120, https://doi.org/10.1021/acsomega.0c00281.

[28] A.M. Holban, C. Farcasiu, O.C. Andrei, A.M. Grumezescu, A.T. Farcasiu, Surface modification to modulate microbial biofilms—applications in dental medicine, Materials 14 (2021), https://doi.org/10.3390/MA14226994.

[29] T. Wei, Z. Tang, Q. Yu, H. Chen, Smart antibacterial surfaces with switchable bacteria-killing and bacteria-releasing capabilities, ACS Appl. Mater. Interfaces 9 (2017) 37511–37523, https://doi.org/10.1021/ACSAMI.7B13565/ASSET/IMAGES/LARGE/AM-2017-13565B_0014.JPEG.

[30] Y.Z. Wan, S. Raman, F. He, Y. Huang, Surface modification of medical metals by ion implantation of silver and copper, Vacuum 81 (2007) 1114–1118, https://doi.org/10.1016/J.VACUUM.2006.12.011.

[31] A. Cochis, B. Azzimonti, C. Della Valle, E. De Giglio, N. Bloise, L. Visai, S. Cometa, L. Rimondini, R. Chiesa, The effect of silver or gallium doped titanium against the multidrug resistant Acinetobacter baumannii, Biomaterials 80 (2016) 80–95, https://doi.org/10.1016/j.biomaterials.2015.11.042.

[32] L. Rimondini, C. Della Valle, A. Cochis, B. Azzimonti, R. Chiesa, The biofilm formation onto implants and prosthetic materials may be contrasted using Gallium (3+), Key Eng. Mater. 587 (2014) 315–320, https://doi.org/10.4028/www.scientific.net/KEM.587.315.

[33] Y. Kaneko, M. Thoendel, O. Olakanmi, B.E. Britigan, P.K. Singh, The transition metal gallium disrupts Pseudomonas aeruginosa iron metabolism and has antimicrobial and antibiofilm activity, J. Clin. Investig. 117 (2007) 877–888, https://doi.org/10.1172/JCI30783.

[34] C.H. Goss, Y. Kaneko, L. Khuu, G.D. Anderson, S. Ravishankar, M.L. Aitken, N. Lechtzin, G. Zhou, D.M. Czyz, K. McLean, O. Olakanmi, H.A. Shuman, M. Teresi, E. Wilhelm, E. Caldwell, S.J. Salipante, D.B. Hornick, R.J. Siehnel, L. Becker, B. E. Britigan, P.K. Singh, Gallium disrupts bacterial iron metabolism and has therapeutic effects in mice and humans with lung infections, Sci. Transl. Med. 10 (2018) 1–12, https://doi.org/10.1126/scitranslmed.aat7520.

[35] A. Cochis, B. Azzimonti, R. Chiesa, L. Rimondini, M. Gasik, Metallurgical gallium additions to titanium alloys demonstrate a strong time-increasing antibacterial activity without any cellular toxicity, ACS Biomater. Sci. Eng. 5 (2019) 2815–2820, https://doi.org/10.1021/acsbiomaterials.9b00147.

[36] E. Xiang, M.N. Gómez-Cerezo, Y. Ali, S.S. Ramachandra, N. Yang, M. Dargusch, C. S. Moran, S. Ivanovski, A. Abdal-Hay, Surface modification of pure zinc by acid etching: accelerating the corrosion rate and enhancing biocompatibility and antibacterial characteristics, ACS Appl. Mater. Interfaces (2022), https://doi.org/10.1021/acsami.2c00918.

[37] Q. Shen, Y. Qi, Y. Kong, H. Bao, Y. Wang, A. Dong, H. Wu, Y. Xu, Advances in copper-based biomaterials with antibacterial and osteogenic properties for bone tissue engineering, Front. Bioeng. Biotechnol. 9 (2022) 1–9, https://doi.org/10.3389/fbioe.2021.795425.

[38] C. Molteni, H.K. Abicht, M. Solioz, Killing of bacteria by copper surfaces involves dissolved copper, Appl. Environ. Microbiol. 76 (2010) 4099, https://doi.org/10.1128/AEM.00424-10.

[39] C.E. Santo, N. Taudte, D.H. Nies, G. Grass, Contribution of copper ion resistance to survival of escherichia coli on metallic copper surfaces, Appl. Environ. Microbiol. 74 (2008) 977, https://doi.org/10.1128/AEM.01938-07.

[40] C.E. Santo, D. Quaranta, G. Grass, Antimicrobial metallic copper surfaces kill Staphylococcus haemolyticus via membrane damage, Microbiologyopen 1 (2012) 46–52, https://doi.org/10.1002/MBO3.2.

[41] R. Hong, T.Y. Kang, C.A. Michels, N. Gadura, Membrane lipid peroxidation in copper alloy-mediated contact killing of Escherichia coli, Appl. Environ. Microbiol. 78 (2012) 1776, https://doi.org/10.1128/AEM.07068-11.

[42] R. Nandakumar, C.E. Santo, N. Madayiputhiya, G. Grass, Quantitative proteomic profiling of the Escherichia coli response to metallic copper surfaces, Biometals 24 (2011) 429–444, https://doi.org/10.1007/S10534-011-9434-5.

[43] Z. Ma, L. Ren, R. Liu, K. Yang, Y. Zhang, Z. Liao, W. Liu, M. Qi, R.D.K. Misra, Effect of heat treatment on Cu distribution, antibacterial performance and cytotoxicity of Ti-6Al-4V-5Cu Alloy, J. Mater. Sci. Technol. 31 (2015) 723–732, https://doi.org/10.1016/J.JMST.2015.04.002.

[44] Y.H. Chang, C.Y. Chao, Y.T. Chang, J.K. Du, Effect of phase distribution on the antibacterial property and cytotoxicity of Ti-5Al-2.5Cu alloy after heat treatment at various temperatures, Metals 2020 10 (10) (2020) 858, https://doi.org/10.3390/MET10070858.

[45] E. Zhang, X. Wang, M. Chen, B. Hou, Effect of the existing form of Cu element on the mechanical properties, bio-corrosion and antibacterial properties of Ti-Cu alloys for biomedical application, Mater. Sci. Eng.: C. 69 (2016) 1210–1221, https://doi.org/10.1016/J.MSEC.2016.08.033.

[46] P. Mahmoudi, M.R. Akbarpour, H.B. Lakeh, F. Jing, M.R. Hadidi, B. Akhavan, Antibacterial Ti–Cu implants: a critical review on mechanisms of action, Mater. Today Bio 17 (2022) 100447, https://doi.org/10.1016/J.MTBIO.2022.100447.

[47] M. Arroussi, C. Bai, J. Zhao, S. Zhang, Z. Xia, Q. Jia, K. Yang, Preliminary study on biocorrosion inhibition effect of Ti-5Cu alloy against marine bacterium Pseudomonas aeruginosa, Appl. Surf. Sci. 578 (2022) 151981, https://doi.org/10.1016/J.APSUSC.2021.151981.

[48] V.K. Manivasagam, G. Perumal, H.S. Arora, K.C. Popat, Enhanced antibacterial properties on superhydrophobic micro-nano structured titanium surface, J. Biomed. Mater. Res A 110 (2022) 1314–1328, https://doi.org/10.1002/JBM.A.37375.

[49] Y.Z. Wan, G.Y. Xiong, H. Liang, S. Raman, F. He, Y. Huang, Modification of medical metals by ion implantation of copper, Appl. Surf. Sci. 253 (2007) 9426–9429, https://doi.org/10.1016/J.APSUSC.2007.06.031.

[50] M. Arroussi, C. Bai, J. Zhao, S. Zhang, Z. Xia, Q. Jia, K. Yang, Preliminary study on biocorrosion inhibition effect of Ti-5Cu alloy against marine bacterium Pseudomonas aeruginosa, Appl. Surf. Sci. 578 (2022) 151981, https://doi.org/10.1016/J.APSUSC.2021.151981.

[51] I. McCue, E. Benn, B. Gaskey, J. Erlebacher, Dealloying and dealloyed materials, Annu Rev. Mater. Res. 46 (2016) 263–286, https://doi.org/10.1146/annurev-matsci-070115-031739.

[52] E. Vassileva, L. Mihaylov, L. Lyubenova, T. Spassov, F. Scaglione, P. Rizzi, Porous metallic structures by dealloying amorphous alloys, J. Alloy. Compd. 969 (2023) 172417, https://doi.org/10.1016/J.JALLCOM.2023.172417.

[53] N. Fernández-Navas, C.J. Querebillo, K. Tiwari, M. Hantusch, V. Shtefan, N. Pérez, P. Rizzi, M. Zimmermann, A. Gebert, Electrochemical surface nanostructuring of Ti47Cu38Fe2.5Zr7.5Sn2Si1Ag2 metallic glass for improved pitting corrosion resistance, Adv. Eng. Mater. (2024) 2302206, https://doi.org/10.1002/ADEM.202302206.

[54] K. Tiwari, A. Blanquer, C. Pavan, M. Tomatis, N.F. Navas, F. Scaglione, G. Fiore, F. Turci, C. Nogués, P. Rizzi, Surface modification of Ti40Cu40Zr11Fe3Sn3Ag3 amorphous alloy for enhanced biocompatibility in implant applications, J. Mater. Res. Technol. 30 (2024) 2333–2346, https://doi.org/10.1016/J.JMRT.2024.03.225.

[55] K. Tiwari, C.J. Querebillo, N. Fernandez-Navas, M.Y. Roshchina, M. Hantusch, C. Pavan, F. Scaglione, G. Fiore, F. Turci, P. Rizzi, A. Gebert, Surface nanostructuring of Ti40Cu40Zr11Fe3Sn3Ag3 amorphous alloy by alkaline chemical treatment for potential use as a biocompatible material, J. Alloy. Compd. 994 (2024) 174703, https://doi.org/10.1016/J.JALLCOM.2024.174703.

[56] F.F. Tuon, L.R. Dantas, P.H. Suss, V.S. Tasca Ribeiro, Pathogenesis of the Pseudomonas aeruginosa Biofilm: a review, Pathogens 11 (2022), https://doi.org/10.3390/PATHOGENS11030300.
[57] R. Yin, J. Cheng, J. Wang, P. Li, J. Lin, Treatment of Pseudomonas aeruginosa infectious biofilms: challenges and strategies, Front. Microbiol. 13 (2022), https://doi.org/10.3389/FMICB.2022.955286.
[58] V. Nandakumar, S. Chittaranjan, V.M. Kurian, M. Doble, Characteristics of bacterial biofilm associated with implant material in clinical practice, Polym. J. 2013 (2012) 137–152, https://doi.org/10.1038/pj.2012.130.
[59] G. Grass, C. Rensing, M. Solioz, Metallic copper as an antimicrobial surface, Appl. Environ. Microbiol. 77 (2011) 1541–1547, https://doi.org/10.1128/AEM.02766-10.
[60] L. Wang, Y. Fu, Q. Li, Z. Wang, EPR evidence for mechanistic diversity of Cu(II)/peroxygen oxidation systems by tracing the origin of DMPO spin adducts, Environ. Sci. Technol. 56 (2022) 8796–8806, https://doi.org/10.1021/ACS.EST.2C00459.
[61] V.N. Shetti, P. Manikandan, D. Srinivas, P. Ratnasamy, Reactive oxygen species in epoxidation reactions over titanosilicate molecular sieves, J. Catal. 216 (2003) 461–467, https://doi.org/10.1016/S0021-9517(02)00119-7.
[62] P. Tengvall, I. Lundström, L. Sjöqvist, H. Elwing, L.M. Bjursten, Titanium-hydrogen peroxide interaction: model studies of the influence of the inflammatory response on titanium implants, Biomaterials 10 (1989) 166–175, https://doi.org/10.1016/0142-9612(89)90019-7.
[63] D.H. Kim, A.D. Bokare, M.S. Koo, W. Choi, Heterogeneous catalytic oxidation of As (III) on nonferrous metal oxides in the presence of H2O2, Environ. Sci. Technol. 49 (2015) 3506–3513, https://doi.org/10.1021/ES5056897.
[64] H.H. Kim, H. Lee, D. Lee, Y.J. Ko, H. Woo, J. Lee, C. Lee, A.L.T. Pham, Activation of hydrogen peroxide by a titanium oxide-supported iron catalyst: evidence for surface Fe(IV) and its selectivity, Environ. Sci. Technol. 54 (2020) 15424–15432, https://doi.org/10.1021/ACS.EST.0C04262.
[65] E. Scarcello, A. Herpain, M. Tomatis, F. Turci, P.J. Jacques, D. Lison, Hydroxyl radicals and oxidative stress: the dark side of Fe corrosion, Colloids Surf. B Biointerfaces 185 (2020), https://doi.org/10.1016/J.COLSURFB.2019.110542.
[66] Q. Chen, Z. Qi, Y. Feng, H. Liu, Z. Wang, L. Zhang, W. Wang, Insight into fast catalytic degradation of neutral reactive red 195 solution by FePC glassy alloy: Fe release and OH generation, J. Mol. Liq. 364 (2022) 120058, https://doi.org/10.1016/J.MOLLIQ.2022.120058.
[67] W. He, Y.T. Zhou, W.G. Wamer, M.D. Boudreau, J.J. Yin, Mechanisms of the pH dependent generation of hydroxyl radicals and oxygen induced by Ag nanoparticles, Biomaterials 33 (2012) 7547–7555, https://doi.org/10.1016/J.BIOMATERIALS.2012.06.076.
[68] M.Yu Roshchina, C.J. Querebillo, E. Dmitrieva, A. Voss, N. Israel, T. Gemming, L. Giebeler, S. Pilz, S. Roeher, V. Hoffmann, M. Hantusch, I.M. Weidinger, A. Gebert, Corrosion behavior of an oxide nanotube-coated β-type Ti-45Nb implant alloy in a simulated inflammatory solution, Corros. Sci. 227 (2024) 111767, https://doi.org/10.1016/J.CORSCI.2023.111767.
[69] M.A. Voinov, J.O.S. Pagán, E. Morrison, T.I. Smirnova, A.I. Smirnov, Surface-mediated production of hydroxyl radicals as a mechanism of iron oxide nanoparticle biotoxicity, J. Am. Chem. Soc. 133 (2011) 35–41, https://doi.org/10.1021/JA104683W.
[70] Y. Cheng, G. Feng, C.I. Moraru, Micro- and nanotopography sensitive bacterial attachment mechanisms: a review, Front. Microbiol. 10 (2019), https://doi.org/10.3389/FMICB.2019.00191.
[71] C.M. Bhadra, V. Khanh Truong, V.T.H. Pham, M. Al Kobaisi, G. Seniutinas, J. Y. Wang, S. Juodkazis, R.J. Crawford, E.P. Ivanova, Antibacterial titanium nano-patterned arrays inspired by dragonfly wings, Sci. Rep. 2015 5:1 5 (2015) 1–12, https://doi.org/10.1038/srep16817.
[72] M. Lorenzetti, I. Dogša, T. Stošicki, D. Stopar, M. Kalin, S. Kobe, S. Novak, The influence of surface modification on bacterial adhesion to titanium-based substrates, ACS Appl. Mater. Interfaces 7 (2015) 1644–1651, https://doi.org/10.1021/AM507148N.
[73] A. Yamamoto, R. Honma, A. Tanaka, M. Sumita, Generic tendency Met. salt Cytotox. Six. Cell lines (1999), https://doi.org/10.1002/(SICI)1097-4636(19991205)47:3.
[74] A. Biesiekierski, J. Wang, M. Abdel-Hady Gepreel, C. Wen, A new look at biomedical Ti-based shape memory alloys, Acta Biomater. 8 (2012) 1661–1669, https://doi.org/10.1016/J.ACTBIO.2012.01.018.
[75] T. Yamazaki, A. Yamazaki, Y. Hibino, S.A. Chowdhury, Y. Yokote, Y. Kanda, S. Kunii, H. Sakagami, H. Nakajima, J. ShimadaBiological Impact of Contact with Metals on Cells, In Vivo (Brooklyn) 20 (2006) 605–611. https://iv.iiarjournals.org/content/20/5/605 (accessed December 3, 2023)..
[76] A. Blanquer, E. Pellicer, A. Hynowska, L. Barrios, E. Ibáñez, M.D. Baró, J. Sort, C. Nogués, In vitro biocompatibility assessment of Ti40Cu 38Zr10Pd12 bulk metallic glass, J. Mater. Sci. Mater. Med. 25 (2014) 163–172, https://doi.org/10.1007/s10856-013-5041-z.
[77] A. Milheiro, K. Nozaki, C.J. Kleverlaan, J. Muris, H. Miura, A.J. Feilzer, In vitro cytotoxicity of metallic ions released from dental alloys, Odontology 104 (2016) 136–142, https://doi.org/10.1007/S10266-014-0192-Z.
[78] H. Chai, L. Guo, X. Wang, Y. Fu, J. Guan, L. Tan, L. Ren, K. Yang, Antibacterial effect of 317L stainless steel contained copper in prevention of implant-related infection in vitro and in vivo, J. Mater. Sci. Mater. Med. 22 (2011) 2525–2535, https://doi.org/10.1007/s10856-011-4427-z.
[79] C.A. Grillo, M.A. Reigosa, M.F. Lorenzo de Mele, Effects of copper ions released from metallic copper on CHO-K1 cells, Mutat. Res. /Genet. Toxicol. Environ. Mutagen. 672 (2009) 45–50, https://doi.org/10.1016/J.MRGENTOX.2008.09.012.
[80] W.S. da Cruz Nizer, V. Inkovskiy, Z. Versey, N. Strempel, E. Cassol, J. Overhage, Oxidative Stress Response in Pseudomonas aeruginosa, Pathogens 10 (2021), https://doi.org/10.3390/PATHOGENS10091187.
[81] M. Ölander, N. Handin, P. Artursson, Image-based quantification of cell debris as a measure of apoptosis, Anal. Chem. 91 (2019) 5548–5552, https://doi.org/10.1021/ACS.ANALCHEM.9B01243/ASSET/IMAGES/LARGE/AC-2019-01243H_0005.JPEG.
[82] S. Huh, D.F.E. Ker, H. Su, T. Kanade, Apoptosis detection for adherent cell populations in time-lapse phase-contrast microscopy images, Med. Image Comput. Comput. Assist Inter. 15 (2012) 331–339, https://doi.org/10.1007/978-3-642-33415-3_41.
[83] D.J. Taatjes, B.E. Sobel, R.C. Budd, Morphological and cytochemical determination of cell death by apoptosis, Histochem Cell Biol. 129 (2008) 33–43, https://doi.org/10.1007/S00418-007-0356-9/FIGURES/4.
[84] C. Nogués, A. Blanquer, L. Barrios, E. Ibañez, Assessment of metallic alloys biocompatibility, Biomater. Clin. Pract.: Adv. Clin. Res. Med. Devices (2017) 461–475, https://doi.org/10.1007/978-3-319-68025-5_16.
[85] E.M. Czekanska, M.J. Stoddart, J.R. Ralphs, R.G. Richards, J.S. Hayes, A phenotypic comparison of osteoblast cell lines versus human primary osteoblasts for biomaterials testing, J. Biomed. Mater. Res. A 102 (2014) 2636–2643, https://doi.org/10.1002/jbm.a.34937.